How to cite: *Angew. Chem. Int. Ed.* **2023,** *62,* e202217076
International Edition: doi.org/10.1002/anie.202217076
German Edition: doi.org/10.1002/ange.202217076

VIP **Enzyme Models** *Very Important Paper*

A New Thiolate-Bound Dimanganese Cluster as a Structural and Functional Model for Class Ib Ribonucleotide Reductases

*Beatrice Battistella, Thomas Lohmiller, Beatrice Cula, Peter Hildebrandt, Uwe Kuhlmann, Holger Dau, Stefan Mebs, and Kallol Ray**

Abstract: In class Ib ribonucleotide reductases (RNRs) a dimanganese(II) cluster activates superoxide ($O_2^{\bullet-}$) rather than dioxygen (O_2), to access a high valent Mn^{III}–O_2–Mn^{IV} species, responsible for the oxidation of tyrosine to tyrosyl radical. In a biomimetic approach, we report the synthesis of a thiolate-bound dimanganese complex $[Mn^{II}_2(BPMT)(OAc)_2](ClO)_4$ (BPMT = (2,6-bis{[bis(2-pyridylmethyl)amino]methyl}-4-methylthiophenolate) (**1**) and its reaction with $O_2^{\bullet-}$ to form a $[(BPMT)MnO_2Mn]^{2+}$ complex **2**. Resonance Raman investigation revealed the presence of an O–O bond in **2**, while EPR analysis displayed a 16-line $S_t = 1/2$ signal at $g = 2$ typically associated with a $Mn^{III}Mn^{IV}$ core, as detected in class Ib RNRs. Unlike all other previously reported Mn–O_2–Mn complexes, generated by $O_2^{\bullet-}$ activation at Mn_2 centers, **2** proved to be a capable electrophilic oxidant in aldehyde deformylation and phenol oxidation reactions, rendering it one of the best structural and functional models for class Ib RNRs.

Introduction

Ribonucleotide reductases (RNRs) catalyze the conversion of ribonucleotides into their corresponding deoxyribonucleotides, which are precursors necessary for DNA synthesis and repair in all organisms.[1–7] Three different classes of RNRs are known, with class I being subdivided into five subclasses (Ia–e).[1,7,8] The RNRs differ in the nature of the stable metallocofactors required for the transient generation of a cysteine thiyl radical (Cys•) that initiates nucleotide reduction. The oxidizing equivalent necessary for reversible Cys• generation is stored as stable tyrosyl (Y•; class Ia, Ib), 5′-deoxyadenosyl (class II) or glycyl radicals (class III), allowing the distinction of three main classes of RNRs.[1] The present study is relevant to the class Ib RNRs that use a dimanganese (Mn^{II}_2) cofactor to promote Y• formation by oxidation of an adjacent tyrosine residue (Tyr_{105}) in the enzymatic β subunit (Scheme 1).[2,7,9–11] The work of Stubbe and co-workers has shown that the Mn^{II}_2 cofactor is unreactive towards O_2 and requires a superoxide anion ($O_2^{\bullet-}$), generated by reduction of O_2 by a flavodoxin protein (flavodoxin hydroquinone, $NrdI_{hq}$), to assemble an oxo-bridged dimanganese(III,IV) species that was identified by rapid freeze quench EPR spectroscopy.[2] The $Mn^{III}Mn^{IV}$ form is then rapidly converted into a Mn^{III}_2-Y• cofactor necessary for Cys• generation. The molecular mechanism by which the $Mn^{III}Mn^{IV}$ form is assembled is unknown, although a transient $Mn^{II}Mn^{III}$-(hydro)peroxide species was proposed as an intermediate (Scheme 1).[1,2]

The investigation of the spectroscopic and reactivity properties of biomimetic model compounds can provide vital insight into the mechanism of enzymatic reactions. Accordingly, numerous model complexes featuring bis(μ-oxo)dimanganese(III,IV) cores that serve as potential mimics of the $Mn^{III}Mn^{IV}$ form of the class Ib RNRs have been synthesized.[12–15] Some of these complexes have been shown to oxidize substrates by a H-atom transfer mechanism, thus mimicking tyrosine oxidation by the $Mn^{III}Mn^{IV}$ form of Mn-RNR.[13,16,17] However, the reported synthetic procedures generally require treatment of mononuclear Mn^{II} complexes with O_2 or H_2O_2, which differs significantly from the proposed enzymatic mechanism involving the reaction between Mn^{II}_2 cofactor and $O_2^{\bullet-}$. Furthermore, the synthesis of $Mn^{II}Mn^{III}$-peroxide moieties has remained elusive, until very recently. Using UV/Vis absorption, EPR, X-ray absorption near-edge (XANES) spectroscopy and reactivity

[*] B. Battistella, Dr. T. Lohmiller, Dr. B. Cula, Prof. Dr. K. Ray
Institut für Chemie, Humboldt-Universität zu Berlin
Brook-Taylor-Straße 2, 12489 Berlin (Germany)
E-mail: kallol.ray@chemie.hu-berlin.de
Dr. T. Lohmiller
EPR4Energy Joint Lab, Department Spins in Energy Conversion and Quantum Information Science, Helmholtz Zentrum Berlin für Materialien und Energie GmbH
Albert-Einstein-Str. 16, 12489 Berlin (Germany)
Prof. Dr. P. Hildebrandt, Dr. U. Kuhlmann
Institut für Chemie, Fakultät II, Technische Universität Berlin
Straße des 17. Juni 135, 10623 Berlin (Germany)
Prof. Dr. H. Dau, Dr. S. Mebs
Institut für Physik, Freie Universität zu Berlin
Arnimallee 14, 14195 Berlin (Germany)

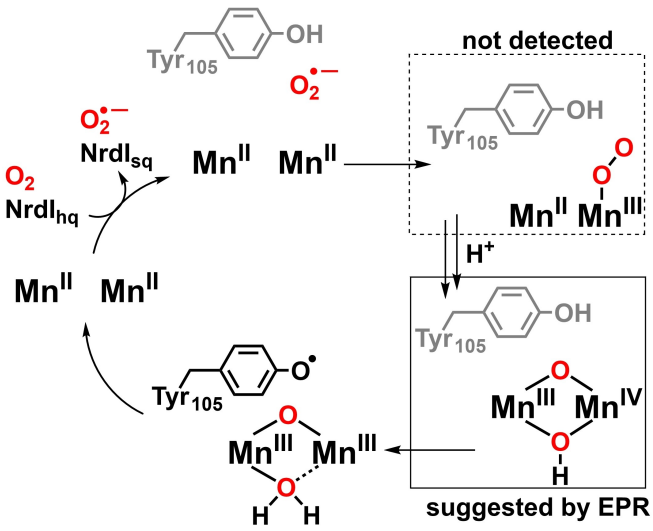

Scheme 1. Proposed mechanism for Y• formation by the enzymatic cofactor of class Ib RNRs from *E. Coli*.[1,4]

studies, McDonald and co-workers provided first evidence for the generation of such species in the reactions of two oxido-bridged dimanganese(II) complexes, $[Mn^{II}_2(OAc)(N\text{-}Et\text{-}HPTB)](ClO_4)_2$ (N-Et-HPTB = *N,N,N′,N′*-tetrakis(2-(1-ethylbenzimidazolyl))-2-hydroxy-1,3-diaminopropane, OAc^- = acetate)[18] and $[Mn^{II}_2(OAc)_2(BPMP)](ClO_4)$ (BPMP = (2,6-bis{[bis(2-pyridylmethyl)amino]methyl}-4-methylphenolate)[19] with $O_2^{\bullet-}$ (Scheme 2). However, an unambiguous assignment of the peroxo-binding by vibrational analysis in both cases was hampered, since no ν(O–O) vibrational mode of the proposed $Mn^{II}Mn^{III}$-peroxide moieties could be detected in the Raman and infrared spectra.

In our continuous efforts to uncover structure–reactivity relationships of metal-dioxygen intermediates, we have now

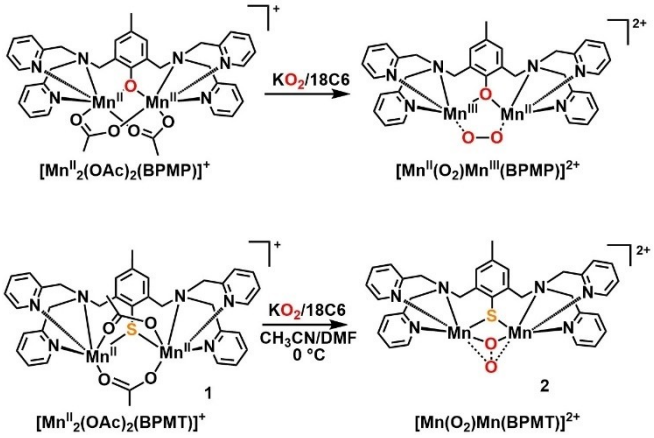

Scheme 2. Reactions of $[Mn^{II}_2(OAc)_2(BPMP)](ClO_4)$[19] and $[Mn^{II}_2(OAc)_2(BPMT)](ClO_4)$ (**1**) complexes with $O_2^{\bullet-}$ to form nucleophilic $[Mn^{II}(O_2)Mn^{III}(BPMP)]]^{2+}$ and electrophilic $[Mn(O_2)Mn(BPMT)]^{2+}$ (**2**) complexes, respectively. 18C6 represents 18-crown-6. Notably, the straightforward assignment of the manganese oxidation states is difficult in **2**.

investigated the reaction of $[Mn^{II}_2(OAc)_2(BPMT)](ClO_4)$ (BPMT = (2,6-bis{[bis(2-pyridylmethyl)amino]methyl}-4-methylthiophenolate) (**1**) with $O_2^{\bullet-}$, whereby the phenolate bridge in the previously reported $[Mn^{II}_2(OAc)_2(BPMP)](ClO_4)$ complex was substituted by thiolate (Scheme 2). Consistent with the crucial role of thiolate moieties in biology, where S-donors are often known to assist in various metal-based electron transfer processes,[20–23] the introduction of sulfur ligation is shown to induce distinct spectroscopic and reactivity properties of the $[Mn_2(BPMT)(O_2)]^{2+}$ (**2**) species formed upon $O_2^{\bullet-}$ activation (Scheme 2). This study, therefore, underlines the importance of subtle electronic changes in the reactivity of the biologically relevant metal-dioxygen intermediates.

Results and Discussion

The BPMT ligand was synthesized as previously described (Figures S1–S6)[24] and it was metalated in CH_3CN under an inert atmosphere by the addition of $Mn(OAc)_2$ (4 equiv; see the Supporting Information). Electron-spray ionization mass spectrometry (ESI-MS) and elemental analysis confirmed the formation and elemental composition of **1** (Figure S7). Further characterization of **1** was performed by X-band EPR and cyclic voltammetric (CV) studies (Figures S8 and S9). The $Mn^{II/II}/Mn^{II/III}$ and $Mn^{II/III}/Mn^{III/III}$ potentials are comparable in **1** and $[Mn^{II}_2(OAc)_2(BPMP)](ClO_4)$.[14,25,26] The CV of **1** shows an additional peak at 0.38 V vs $Fc^{+/0}$, which based on the CV of the $[Zn^{II}_2(OAc)(BPMT)]^{2+}$ complex (Tables S1 and S2)[29] is attributed to the non-innocence of the BPMT ligand. Single crystals suitable for X-ray diffraction (XRD) analysis of **1** were grown from CH_3CN by diethyl ether vapor diffusion. Compound **1** was found to consist of two six-coordinate Mn^{II} atoms, both with a distorted octahedral geometry (Figure 1a) and bridged by two acetate ligands in a *syn–anti*[27,28] conformation and a BPMT–thiophenolate moiety. The thiophenolate donor in **1** is symmetrically bound to the two manganese sites (average

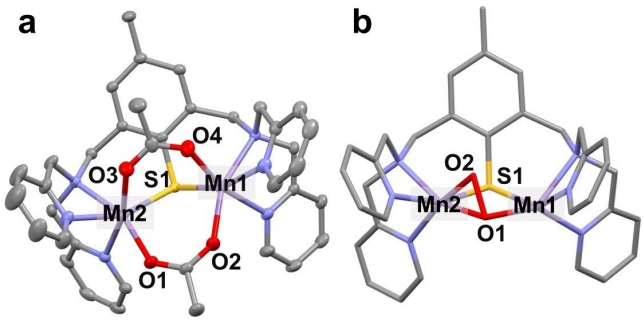

Figure 1. a) XRD determined molecular structure of $[Mn^{II}_2(OAc)_2(BPMT)](ClO_4)$ (**1**).[29] Hydrogen atoms, solvent molecules (CH_3CN) and perchlorate anions are omitted for the sake of clarity. Selected distances: Mn(1)–S(1) = 2.590(1) Å, Mn(1)–O(2) = 2.105(2) Å, Mn(1)–O(4) = 2.130(2) Å; Mn(2)–S(1) = 2.5892(6) Å; Mn(2)–O(1) = 2.108(2) Å; Mn(2)–O(5) = 2.138(2) Å; Mn(1)–Mn(2) = 3.541 Å. See Table S3 for further bond lengths and bond angles. b) DFT optimized structure of **2**. Color code: C gray, N blue, O red, S yellow, Mn purple.

Mn–S = 2.59 Å), with a bond length approximately 0.5 Å longer than the Mn–O(phenolate) in $[Mn^{II}_2(OAc)_2(BPMP)]^+$ (average Mn–O = 2.11 Å),[28] and a significantly smaller Mn–S–Mn angle of 86.25° relative to the Mn–O–Mn angle of 107.9° in $[Mn^{II}_2(OAc)_2(BPMP)]^+$ (Tables S1 and S3). Compound **1** displayed a Mn···Mn separation of 3.541 Å, which is longer than the value of 3.412 Å reported for $[Mn^{II}_2(OAc)_2(BPMP)]^+$.[28]

Following the procedure reported previously for the generation of $[Mn^{II}(O_2)Mn^{III}(N\text{-}Et\text{-}HPTB)]^{2+}$ [18] and $[Mn^{II}(O_2)Mn^{III}(BPMP)]^{2+}$,[19] a solution in CH_3CN containing complex **1** (1.5 mM, cooled to 0 °C) was treated with a solution in *N*,*N*-dimethylformamide (DMF, 0.1 mL) containing KO_2 (3 equiv) and 18-crown-6 (9 equiv; 18C6 = 1,4,7,10,13,16-hexaoxacyclooctadecane; Scheme 2). The formation (within 3 min) of a brown species **2** with a half-life ($t_{1/2}$) of 200 min at 0 °C (Figure S10a) was observed with no distinct absorption bands (Figure 2a). Notably, the broad feature in the absorption spectrum of **2** is significantly different to that reported for $[Mn^{II}(O_2)Mn^{III}(BPMP)]^{2+}$ [19] and other Mn^{III}-peroxo[30] complexes, and rather matches the absorption spectra observed for (bis-μ-oxo)$Mn^{III}Mn^{IV}$[12,13] and $Mn^{IV}Mn^{IV}$ cores.[16,17,31] Interestingly, the absorption spectrum of **2** also bears significant resemblance to the spectrum reported for the CmlI-peroxo intermediate in chloroamphenicol (CmlI),[32,43] where the distinct spectroscopic properties of the intermediate have been controversially attributed to the presence of unusual (μ-1,1)peroxo or μ-η^1:η^2-peroxo binding modes, rather than the more typical μ-η^1:η^1- and μ-η^2:η^2-peroxo ligations observed in other non-heme oxygenases (see inset in Figure 2c for possible peroxo binding modes).[4]

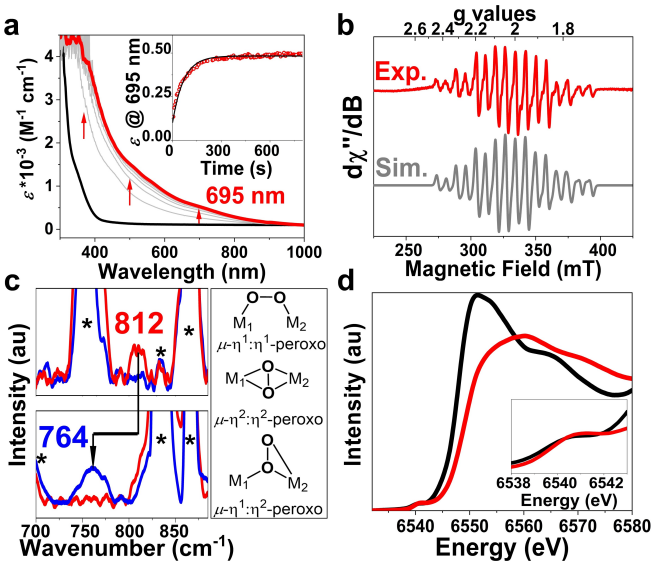

Figure 2. a) UV-Vis spectral changes associated with the reaction of **1** (black line) with 3 equivalents of KO_2 at 0 °C in CH_3CN to form **2** (red line). The time trace of the development of the band at 695 nm is shown in the inset. b) X-band EPR spectrum of **2** in 1:9 DMF/CH_3CN (9.363 GHz, 1 mW, 13 K; red) and simulated spectrum (gray). c) rRaman spectra of 6 mM **2** in 1:9 DMF/CH_3CN (top) and 1:9 DMF/CD_3CN (bottom) at −30 °C, upon excitation at 406 nm. The spectra in presence of $^{16}O_2^{\bullet-}$ and $^{18}O_2^{\bullet-}$ are shown in red and blue, respectively; the solvent peaks are labelled with asterisks. Possible binding modes of a peroxo ligand to a dimetallic cluster are shown in the inset. d) 1s→4p transitions in the Mn *K*-edge XAS spectra of **1** (black) and **2** (red) in a 1:9 DMF/CH_3CN frozen solution at 20 K; the 1s→3d pre-edge transitions are shown in the inset.

The conversion of **1** into **2** is associated with the appearance of a total spin $S_t = 1/2$ EPR signal centered at $g \approx 2$ with well resolved ^{55}Mn hyperfine features (Figure 2b) as observed for mixed-valent Mn dimers.[33] Both the spectral width and shape of the $g \approx 2$ signal closely resemble the typical appearance of the numerous reported $Mn^{III}Mn^{IV}$ centers, both synthetic and biological.[2,12,14,27,34,35] The width of 125 mT is characteristic for $Mn^{III}Mn^{IV}$ X-band spectra, while $Mn^{II}Mn^{III}$ systems show a greater width variability of at least 180 mT throughout.[18,19,26,27,35,36] The hyperfine pattern is dominated by 16-lines, as commonly observed for $Mn^{III}Mn^{IV}$ species, resulting from spectral overlap of the nominal 36 transitions (assuming isotropic ^{55}Mn *A* tensors). In contrast, $Mn^{II}Mn^{III}$ species tend to display a larger number of lines owing to less overlap over the extended spectral width. Thus, the signal is also significantly different from the 29-line EPR signal reported for $[Mn^{II}(O_2)Mn^{III}(BPMP)]^{2+}$.[19] Besides, a less intense EPR feature at $g \approx 4$ (Figure S9b) is also observed for **2**, possibly due to thermal population of an $S_t = 3/2$ excited state at 13 K of the mixed-valent Mn dimer, as typically observed for weakly coupled $Mn^{II}Mn^{III}$ complexes.[19,26,27] EPR spectral simulation with optimized effective ($S_t = 1/2$) parameters $g^{eff}_{\perp} = 1.996$, $g^{eff}_{||} = 1.993$, $|A(Mn_A)_{\perp,||}| = [451, 389]$ MHz and $|A(Mn_B)_{\perp,||}| = [215, 208]$ MHz gave an excellent match with the experimental signal (Figure 2b). Remarkably, the hyperfine constants closely resemble those detected by Stubbe and co-workers for the enzymatic $Mn^{III}Mn^{IV}$ cofactor ($g^{eff} \approx 2.0$, $A(Mn_A)_{x,y,z} = [-465, -435, -310]$ MHz; $A(Mn_B)_{x,y,z} = [230, 230, 240$ MHz]) in class Ib RNR.[2] Similar values of the *g* and *A* tensors have also been reported for other synthetic $Mn^{III}Mn^{IV}$ clusters.[12,14,37] To further investigate the electronic configuration of each Mn center in **2**, the spin-projection coefficients were taken into account allowing determination of the intrinsic hyperfine coupling constants for **2**, considering both the $Mn^{II}Mn^{III}$ or $Mn^{III}Mn^{IV}$ electronic structures (see Supporting Information).[37,38] Accordingly, the isotropic values of the intrinsic hyperfine tensors are equal to $|a_{iso}| =$ 185 and 160 MHz when **2** is assigned as $Mn^{II}Mn^{III}$. While one metal ion is consistent with Mn^{III} (typical $|a_{iso}| = 165$–225 MHz),[39] the hyperfine interactions of a Mn^{II} center are significantly larger than those obtained for **2** (typical $|a_{iso}| =$ 236–263 MHz). For **2** considered as a $Mn^{III}Mn^{IV}$, $|a_{iso}| = 215$ and 213 MHz were calculated, which are consistent with the presence of one Mn^{III} and one Mn^{IV} center (typical $|a_{iso}| =$ 187–253 MHz).

The resonance Raman (rR) spectra of the reaction mixture of **1** and $O_2^{\bullet-}$ display a vibrational band at 812 cm^{-1}, which is downshifted to 764 cm^{-1} upon ^{18}O labelling (Figure 2c). The 812 cm^{-1} band with an isotopic shift of 48 cm^{-1} (calculated shift $^{16/18}\Delta_{calc.} = 47$ cm^{-1}) is assigned to the O–O stretching mode ($\nu_{O\text{-}O}$) of a peroxo ligand in **2**. Notably, no metal-oxygen stretching mode expected between 500 and

$600\,cm^{-1}$ could be detected for **2**. Possibly, this mode is masked by an intense band at $490\,cm^{-1}$ (Figure S11). While (μ-η^1:η^1)peroxo-metal complexes (Figure 2c, inset) typically exhibit $\nu_{O\text{-}O}$ in the range from 800 to $850\,cm^{-1}$,[4,30,40,41] such an assignment can be excluded for **2** in view of its UV/Vis absorption spectrum, which differs significantly from the spectra typically associated with (μ-η^1:η^1)peroxo-metal cores (Table S4). The observed $\nu_{O\text{-}O}$ mode at $812\,cm^{-1}$ of **2** is also outside the range of values (710–$770\,cm^{-1}$) reported for complexes containing a (μ-η^2:η^2)peroxo binding motif (Table S4).[40,42] However, an alternative (μ-1,1)peroxo binding motif, albeit unknown in manganese chemistry, was reported for a diferric core in the CmlI-peroxo intermediate (originally proposed as (μ-η^1:η^2)peroxo), which shows $\nu_{O\text{-}O}$ = $791\,cm^{-1}$ and broad UV/Vis absorption bands comparable to **2**.[32,43] Indeed, the DFT optimized structure of **2** reveals the presence of a (μ-η^1:η^2)peroxo binding mode in the lowest energy $S_t = 1/2$ state (Figure 1b, Table S5). As depicted in Figure 1b, while one of the peroxo oxygen atoms (O1) bridges the two metal centers (Mn1–O1 = 2.168 Å and Mn2–O1 = 1.947 Å), the other oxygen atom (O2) is bound solely to the Mn^{III} center (Mn2–O2 = 1.836 Å). This results in pentacoordinated (5C) Mn^{II} (=Mn1) and 6 C Mn^{III} (= Mn2) centers in **2**. However, the calculated ν(O–O) for the lowest energy geometry was overestimated by $176\,cm^{-1}$, which was also found previously.[44,45] We therefore employed a geometry scan of the O–O bond length, which yielded a relatively flat surface potential. The energy of the structure exhibiting d(O–O) = 1.485 Å was found to be higher by only $1\,kcal\,mol^{-1}$ as compared to the freely optimized structure. A constrained geometry optimization with an O–O distance fixed at 1.485 Å provided a potential structure for **2** and a calculated ν(O–O) stretch of $814\,cm^{-1}$, which is very close to the experimental data.

X-ray absorption spectroscopic (XAS) studies at the Mn *K*-edge were performed to obtain further insight into the Mn oxidation states in **2**. Figure 2d depicts a comparison of the normalized Mn *K*-edge XAS spectra of **2** with the Mn^{II} precursor complex **1**. A blue shift of ca. 1.9 eV in the edge energy from **1** (6546.9 eV) to **2** (6548.8 eV) was observed, which is significantly larger than the reported approximately 1.0 eV blue shift[19] associated with the formation of $[Mn^{II}(O_2)Mn^{III}(BPMP)]^{2+}$ from $[Mn^{II}_2(OAc)_2(BPMP)](ClO_4)$. However, comparison with manganese–oxo standards of known oxidation states agrees with an overall oxidation state of +2.6 for **2**, plausibly hinting at a $Mn^{II}Mn^{III}$ assignment (Figure S12a). Furthermore, the 1s-to-3d pre-edge transition was found at identical energy (6540.8 eV) in **1** and **2** (Figure 2d, inset).

In an effort to obtain structural information for **1** and **2**, extended X-ray absorption fine structure (EXAFS) analysis was performed (Figure S12b). The EXAFS fit for **1** in solid and solvated states well-resembled the XRD-determined bond lengths, pointing to minor changes in the complex geometry upon solvation (Table S6). The EXAFS features obtained for **2** could be best simulated by the presence of a new short Mn–O scatterer at 1.84 Å and overall shorter bond lengths than in **1**, as predicted upon Mn^{II} oxidation in **1** (Table S6).[46] The EXAFS determined metrical parameters were found to be in reasonable agreement with the DFT calculated structures of both **1** (Figure S13, Table S7) and **2** (Figure 1b, Table S8).

The reactivity of **2** was then investigated in reactions with 2-phenylpropionaldehyde (2-PPA), cyclohexanecarboxaldehyde (CCA) and 4-substituted benzaldehydes (4-X-$C_6H_4C(H)O$ with X = OH, OMe, Me, H) as substrates. Previous work showed that $Mn^{II}Mn^{III}$-peroxo complexes react with aldehydes to give the corresponding deformylated products by attacking the carbonyl group in a nucleophilic reaction.[19] Upon addition of 2-PPA to **2** in CH_3CN at 0 °C, the intermediate decayed immediately and led to acetophenone as the product in quantitative yield, based on the concentration of **2** (Figures S14 and S15). Employment of ^{18}O-labelled **2** led to incorporation of ^{18}O in the acetophenone product (Figure S16). EPR analysis of a solution of **2** after treatment with an excess of 2-PPA, showed a signal ascribable to an integer spin species (Figure S17). This is likely given by two antiferromagnetically coupled Mn^{II} centers as detected for **1**, suggesting the restoration of a reduced form of the dimanganese cluster after substrate oxidation (Scheme S1). The pseudo first-order rate constant of the decay of **2** increased linearly with increasing 2-PPA concentration, thus giving a second-order rate constant of $0.257\,M^{-1}s^{-1}$ (Figures 3a and S14). When α-[D_1]-PPA (ca. 90 %, D-enriched) was used in the reaction, we determined a second-order rate constant of $0.122\,M^{-1}s^{-1}$ (Figure 3a). Therefore, our kinetic studies establish that the $[Mn(O_2)Mn(BPMT)]^{2+}$ complex reacts with 2-PPA through rate-determining hydrogen-atom abstraction (HAA) from the α-position with a kinetic isotope effect (KIE) of 2.1 (Figure 3a, Scheme S1). Further evidence for the electrophilic aldehyde oxidation capability of **2** was obtained by treating **2** with 2-

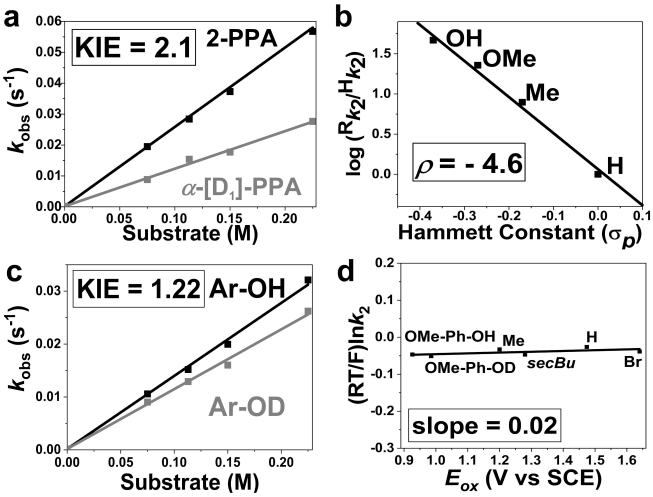

Figure 3. a) Plot of k_2 for the reaction of **2** towards 2-PPA (black) and α-[D_1]-PPA (gray), displaying a KIE value of 2.1. b) Hammett plot for the oxidation of 4-substituted benzaldehydes 4-X-$C_6H_4C(H)O$ (X = OH, OMe, Me, H) by **2** in 1:9 DMF/CH_3CN solution at 0 °C. c) Plot of k_2 for the reaction of **2** towards 4-OMe-2,6-DTBP-OH (Ar–OH, black) and a deuterated analogue (Ar-OD, gray) showing a KIE value of 1.22. d) Plot of (RT/F)ln k_2 against the oxidation potentials (E_{ox}) of the substrates for the reaction of substituted phenols with **2** in CH_3CN at 0 °C.

PPA in the presence of an excess of a radical scavenger, such as CBr_4.[47] The result revealed the preferred formation of 2-bromo-2-phenylpropanal instead of acetophenone as detected by GC-MS, likely due to the radical coupling between $Br^{\bullet}$ and 2-PPA$^{\bullet}$, which was generated after the initial HAA step (Figure S18).[47–49] The presence of an electrophilic O_2^{2-} unit in **2** was further evidenced in its reaction with 4-substituted benzaldehydes (Figures S19–S22). The rate of the reactions increased proportionally with the increasing electron density on the substrate, yielding a negative slope in the Hammett plot ($\rho = -4.6$) further confirming an electrophilic aldehyde oxidation mechanism (Figure 3b).[49,50] Complex **2** also reacted with CCA with a k_2 value of $0.083\ M^{-1}s^{-1}$ at 0 °C, leading to the quantitative formation of cyclohexanecarboxylic acid (Figures S23 and S24).

For a better understanding of the electrophilic reactivity of **2**, we investigated its reactivity with different substituted phenols (Figures S25–S31). The reaction of **2** with 2,6-di-*tert*-butylphenol (2,6-DTBP) led to the formation of the four-electron oxidized substituted dibenzoquinone in 53 % yield based on the concentration of **2**, as determined by GC-MS analysis (Figure S32). While **2** reacts with 2,6-DTBP with $k_2 = 0.33\ M^{-1}s^{-1}$ at 0 °C, the reaction with 2,4-di-*tert*-butylphenol (2,4-DTBP) occurs more than 20 times slower under the same conditions ($k_2 = 0.014\ M^{-1}s^{-1}$), yielding the corresponding C–C coupled product in modest yield (Figure S33, Table S9). To provide deeper insight into the O–H bond activation mechanism towards substituted phenols, KIE studies were performed and the Brønsted/Tafel analogy published by Ram and Hupp[51] for electron transfer processes was applied. Studies on the oxidation of 2,6-di-*tert*-butyl-4-methoxyphenol (4-OMe-2,6-DTBP) by **2** yielded a KIE value of 1.22 corroborating the involvement of proton transfer in the rate-determining step (Figure 3c, S35, and S36). Furthermore, k_2 values (Table S9) were determined for the reactions of **2** with different substituted phenols (ArOH), which when correlated to the ArOH/ArOH$^+$ potentials (E_{ox}) of the phenols afforded a good linear correlation for the $(RT/F)\ln k_2$ versus E_{ox} plot with a slope of 0.02 (Figure 3d). A weak dependence of k_2 on $E_{ox,}$ together with the low observed KIE value, can be attributed to a predominant proton coupled electron transfer (PCET) mechanism, for the oxidation of Ar–OH (Scheme S2).[52–54]

Conclusion

In summary, we have reported the generation of a thiophenolate-bridged $[MnO_2Mn]^{3+}$ core in **2** through a mechanism reminiscent of the $O_2^{\bullet-}$ activation process in biology. Complex **2** exhibits a 16-line $S_t = 1/2$ EPR signal at $g = 2$, which is typically associated with a bis(μ-oxo)$Mn^{III}Mn^{IV}$ core, as formed upon O–O bond cleavage of $O_2^{\bullet-}$ in class Ib RNRs. Complex **2**, however, contains an intact O–O bond as evident from rRaman studies, which may reveal the presence of a peroxo-bridged $Mn^{II}Mn^{III}$ species. Notably, the Mn–S distances in **1** and **2** differ by only 0.04 Å, consistent with our DFT structure for **2**. The unique spectroscopic properties of **2** can be plausibly attributed to the unusual μ-η^1:η^2 binding mode of the peroxo ligand, and the strong covalency of the thiophenolate-bridged $[MnO_2Mn]^{3+}$ core, which makes straightforward assignment of the manganese oxidation states difficult. The effect of sulfur ligation in **2** is also reflected in its ability to oxidize aldehydes, whereby a switch from a predominantly nucleophilic $[MnO_2Mn]^{3+}$ species (in the presence of a phenolate bridge) to an electrophilic $[MnO_2Mn]^{3+}$ core (in the presence of a thiophenolate bridge) is noted. Complex **2** can also oxidize phenols by a PCET mechanism, thereby making it one of the best structural and functional models known to date for the plausible reactive intermediates in class Ib RNRs.

Acknowledgements

We thank the Deutsche Forschungsgemeinschaft (DFG; German Research Foundation) for financial support under Germany's Excellence Strategy—EXC-2033 390677874—"RESOLVE") and EXC-2008—390540038—"UniSysCat", as well as for support to T.L. (Project No. LO 2898/1-1). We acknowledge the Helmholtz Zentrum Berlin (HZB) for providing experimental infrastructure and allocating beamtime at beamline KMC-3 of the BESSY synchrotron, as well as for the X-band EPR measurements. Furthermore, we acknowledge Prof. Dr. W. Nam (Ewha Womens University, Seoul, South Korea) for providing the ^{18}O-labelled oxidant required for the rR spectroscopic analysis of **2** and M. Jux and D. Kass for the rR data collection. Open Access funding enabled and organized by Projekt DEAL.

Conflict of Interest

The authors declare no conflict of interest.

Data Availability Statement

The data that support the findings of this study are available on request from the corresponding author. The data are not publicly available due to privacy or ethical restrictions.

Keywords: Bioinorganic Chemistry · Dimanganese Cofactor · Enzyme Models · Phenol Oxidation · Ribonucleotide Reductases

[1] J. A. Cotruvo, J. Stubbe, *Annu. Rev. Biochem.* **2011**, *80*, 733–767.
[2] J. A. Cotruvo, T. A. Stich, R. D. Britt, J. Stubbe, *J. Am. Chem. Soc.* **2013**, *135*, 4027–4039.
[3] B. L. Greene, G. Kang, C. Cui, M. Bennati, D. G. Nocera, C. L. Drennan, J. Stubbe, *Annu. Rev. Biochem.* **2020**, *89*, 45–75.
[4] B. Battistella, K. Ray, *Coord. Chem. Rev.* **2020**, *408*, 213176.
[5] M. Jayachandran, J. Yoon, J. Wu, D. Cipurko, J. Quon, O. Makhlynets, *Metallomics* **2021**, *13*, mfab062.

[6] J. Stubbe, W. A. van der Donk, *Chem. Rev.* **1998**, *98*, 705–762.
[7] T. B. Ruskoski, A. K. Boal, *J. Biol. Chem.* **2021**, *297*, 101137.
[8] S. Licht, G. J. Gerfen, J. Stubbe, *Science* **1996**, *271*, 477–481.
[9] A. Willing, H. Follmann, G. Auling, *Eur. J. Biochem.* **1988**, *170*, 603–611.
[10] J. A. Cotruvo, J. Stubbe, *Biochemistry* **2010**, *49*, 1297–1309.
[11] J. A. Cotruvo, J. Stubbe, *Biochemistry* **2011**, *50*, 1672–1681.
[12] L. Dubois, R. Caspar, L. Jacquamet, P.-E. Petit, M.-F. Charlot, C. Baffert, M.-N. Collomb, A. Deronzier, J.-M. Latour, *Inorg. Chem.* **2003**, *42*, 4817–4827.
[13] D. F. Leto, S. Chattopadhyay, V. W. Day, T. A. Jackson, *Dalton Trans.* **2013**, *42*, 13014–13025.
[14] P. Huang, A. Magnuson, R. Lomoth, M. Abrahamsson, M. Tamm, L. Sun, B. van Rotterdam, J. Park, L. Hammarström, B. Åkermark, et al., *J. Inorg. Biochem.* **2002**, *91*, 159–172.
[15] H. M. Johnston, D. M. Freire, C. Mantsorov, N. Jamison, K. N. Green, *Eur. J. Inorg. Chem.* **2022**, e202200039.
[16] V. L. Pecoraro, M. J. Baldwin, A. Gelasco, *Chem. Rev.* **1994**, *94*, 807–826.
[17] A. J. Wu, J. E. Penner-Hahn, V. L. Pecoraro, *Chem. Rev.* **2004**, *104*, 903–938.
[18] A. M. Magherusan, A. Zhou, E. R. Farquhar, M. García-Melchor, B. Twamley, L. Que, Jr., A. R. McDonald, *Angew. Chem. Int. Ed.* **2018**, *57*, 918–922; *Angew. Chem.* **2018**, *130*, 930–934.
[19] A. M. Magherusan, S. Kal, D. N. Nelis, L. M. Doyle, E. R. Farquhar, L. Que, Jr., A. R. McDonald, *Angew. Chem. Int. Ed.* **2019**, *58*, 5718–5722; *Angew. Chem.* **2019**, *131*, 5774–5778.
[20] J. A. Kovacs, *Chem. Rev.* **2004**, *104*, 825–848.
[21] A. Dey, M. Chow, K. Taniguchi, P. Lugo-Mas, S. Davin, M. Maeda, J. A. Kovacs, M. Odaka, K. O. Hodgson, B. Hedman, et al., *J. Am. Chem. Soc.* **2006**, *128*, 533–541.
[22] E. I. Solomon, S. I. Gorelsky, A. Dey, *J. Comput. Chem.* **2006**, *27*, 1415–1428.
[23] J. Liu, S. Chakraborty, P. Hosseinzadeh, Y. Yu, S. Tian, I. Petrik, A. Bhagi, Y. Lu, *Chem. Rev.* **2014**, *114*, 4366–4469.
[24] S. Torelli, M. Orio, J. Pécaut, H. Jamet, L. Le Pape, S. Ménage, *Angew. Chem. Int. Ed.* **2010**, *49*, 8249–8252; *Angew. Chem.* **2010**, *122*, 8425–8428.
[25] G. Eilers, C. Zettersten, L. Nyholm, L. Hammarström, R. Lomoth, *Dalton Trans.* **2005**, 1033–1041.
[26] H. Diril, H. R. Chang, M. J. Nilges, X. Zhang, J. A. Potenza, H. J. Schugar, S. S. Isied, D. N. Hendrickson, *J. Am. Chem. Soc.* **1989**, *111*, 5102–5114.
[27] P. J. Pessiki, S. V. Khangulov, D. M. Ho, G. C. Dismukes, *J. Am. Chem. Soc.* **1994**, *116*, 891–897.
[28] S. Blanchard, G. Blondin, E. Rivière, M. Nierlich, J.-J. Girerd, *Inorg. Chem.* **2003**, *42*, 4568–4578.
[29] Deposition Number 2212968 contains the supplementary crystallographic data for this paper. These data are provided free of charge by the joint Cambridge Crystallographic Data Centre and Fachinformationszentrum Karlsruhe Access Structures service.
[30] M. K. Coggins, X. Sun, Y. Kwak, E. I. Solomon, E. Rybak-Akimova, J. A. Kovacs, *J. Am. Chem. Soc.* **2013**, *135*, 5631–5640.
[31] D. Brazzolotto, F. G. Cantú Reinhard, J. Smith-Jones, M. Retegan, L. Amidani, A. S. Faponle, K. Ray, C. Philouze, S. P. de Visser, M. Gennari, et al., *Angew. Chem. Int. Ed.* **2017**, *56*, 8211–8215; *Angew. Chem.* **2017**, *129*, 8323–8327.
[32] T. M. Makris, V. V. Vu, K. K. Meier, A. J. Komor, B. S. Rivard, E. Münck, L. Que, J. D. Lipscomb, *J. Am. Chem. Soc.* **2015**, *137*, 1608–1617.
[33] Double integration of the signal at $g \approx 2$ and comparison with the area of 1 mM Cu^{II} standard measured under the same experimental conditions (Figure S9) suggests a 50 % yield of the intermediate **2**.
[34] K.-O. Schäfer, R. Bittl, F. Lendzian, V. Barynin, T. Weyhermüller, K. Wieghardt, W. Lubitz, *J. Phys. Chem. B* **2003**, *107*, 1242–1250.
[35] C. Teutloff, K.-O. Schäfer, S. Sinnecker, V. Barynin, R. Bittl, K. Wieghardt, F. Lendzian, W. Lubitz, *Magn. Reson. Chem.* **2005**, *43*, S51–S64.
[36] H. Diril, H. R. Chang, X. Zhang, S. K. Larsen, J. A. Potenza, C. G. Pierpont, H. J. Schugar, S. S. Isied, D. N. Hendrickson, *J. Am. Chem. Soc.* **1987**, *109*, 6207–6208.
[37] N. Cox, W. Ames, B. Epel, L. V. Kulik, L. Rapatskiy, F. Neese, J. Messinger, K. Wieghardt, W. Lubitz, *Inorg. Chem.* **2011**, *50*, 8238–8251.
[38] T. Lohmiller, W. Ames, W. Lubitz, N. Cox, S. K. Misra, *Appl. Magn. Reson.* **2013**, *44*, 691–720.
[39] T. Lohmiller, V. Krewald, A. Sedoud, A. W. Rutherford, F. Neese, W. Lubitz, D. A. Pantazis, N. Cox, *J. Am. Chem. Soc.* **2017**, *139*, 14412–14424.
[40] L. M. Mirica, X. Ottenwaelder, T. D. P. Stack, *Chem. Rev.* **2004**, *104*, 1013–1045.
[41] A. J. Jasniewski, L. Que, *Chem. Rev.* **2018**, *118*, 2554–2592.
[42] E. I. Solomon, J. W. Ginsbach, D. E. Heppner, M. T. Kieber-Emmons, C. H. Kjaergaard, P. J. Smeets, L. Tian, J. S. Woertink, *Faraday Discuss.* **2011**, *148*, 11–39.
[43] A. J. Jasniewski, A. J. Komor, J. D. Lipscomb, L. Que, *J. Am. Chem. Soc.* **2017**, *139*, 10472–10485.
[44] B. Battistella, K. Warm, B. Cula, B. Lu, P. Hildebrandt, U. Kuhlmann, H. Dau, S. Mebs, K. Ray, *J. Inorg. Biochem.* **2022**, *227*, 111668.
[45] B. Battistella, L. Iffland-Mühlhaus, M. Schütze, B. Cula, U. Kuhlmann, H. Dau, P. Hildebrandt, T. Lohmiller, S. Mebs, U.-P. Apfel, et al., *Angew. Chem. Int. Ed.* **2023**, *62*, e202214074; *Angew. Chem.* **2023**, *135*, e202214074.
[46] A. Magnuson, P. Liebisch, J. Högblom, M. F. Anderlund, R. Lomoth, W. Meyer-Klaucke, M. Haumann, H. Dau, *J. Inorg. Biochem.* **2006**, *100*, 1234–1243.
[47] F. G. Cantú Reinhard, P. Barman, G. Mukherjee, J. Kumar, D. Kumar, D. Kumar, C. V. Sastri, S. P. de Visser, *J. Am. Chem. Soc.* **2017**, *139*, 18328–18338.
[48] P. Barman, P. Upadhyay, A. S. Faponle, J. Kumar, S. S. Nag, D. Kumar, C. V. Sastri, S. P. de Visser, *Angew. Chem. Int. Ed.* **2016**, *55*, 11091–11095; *Angew. Chem.* **2016**, *128*, 11257–11261.
[49] U. K. Bagha, J. K. Satpathy, G. Mukherjee, C. V. Sastri, S. P. de Visser, *Org. Biomol. Chem.* **2021**, *19*, 1879–1899.
[50] W. Zhu, S. Jang, J. Xiong, R. Ezhov, X.-X. Li, T. Kim, M. S. Seo, Y.-M. Lee, Y. Pushkar, R. Sarangi, Y. Guo, W. Nam, *J. Am. Chem. Soc.* **2021**, *143*, 15556–15561.
[51] M. S. Ram, J. T. Hupp, *J. Phys. Chem.* **1990**, *94*, 2378–2380.
[52] T. Osako, K. Ohkubo, M. Taki, Y. Tachi, S. Fukuzumi, S. Itoh, *J. Am. Chem. Soc.* **2003**, *125*, 11027–11033.
[53] M. H. V. Huynh, T. J. Meyer, *Chem. Rev.* **2007**, *107*, 5004–5064.
[54] J. Y. Lee, R. L. Peterson, K. Ohkubo, I. Garcia-Bosch, R. A. Himes, J. Woertink, C. D. Moore, E. I. Solomon, S. Fukuzumi, K. D. Karlin, *J. Am. Chem. Soc.* **2014**, *136*, 9925–9937.

Manuscript received: November 20, 2022
Accepted manuscript online: December 30, 2022
Version of record online: February 14, 2023